Multi-Scale Modeling and Simulation of DFIG-Based Wind Energy Conversion System

Yue Xia, Ying Chen, *Member, IEEE*, Yankan Song, and Kai Strunz

***Abstract*—A multi-scale transients model of a doubly fed induction generator (DFIG)-based wind energy conversion system (WECS) is developed, implemented, and validated. All ac circuit and control quantities of the electrical part are modeled by analytic signals rather than just real signals. In addition to the real parts, the analytic signals also comprise orthogonal imaginary parts. While measured Fourier spectra of real ac quantities involve positive and negative frequency components, they only involve positive frequency components when extended and represented as analytic signals. With the introduced shift frequency operator, the analytic signal can now be shifted in the frequency domain to reduce its maximum frequency contents and thus allow for a larger time-step size in accordance with the Nyquist criterion. If the shift frequency is set equal to the ac fundamental frequency, then the affiliated ac voltages and currents become dynamic phasors. At a zero shift, however, instantaneous signals can be tracked as in an electromagnetic transients program (EMTP). This is illustrated here for the voltage sourced converters (VSC) of the WECS. By appropriate selection of the shift frequency, both electromagnetic and electromechanical transients are simulated efficiently. Studies involving wind power fluctuations, three-phase-to-ground fault and single-phase-to-ground fault confirm these claims.**

***Index Terms*—Doubly fed induction generator (DFIG), electromagnetic transients, electromechanical transients, multi-scale, interface, voltage-sourced converter (VSC), wind energy conversion system (WECS).**

I. Introduction

WIND power is widely distributed and renewable, and thus produces no greenhouse gases during operation [1]. According to the Global Wind Energy Council's report, the installed wind power capacity worldwide reached 591 GW by the end of 2018 [2]. At the same time, wind energy conversion systems (WECS) modify power system transients over a wide range of frequencies. This observation motivates the development of accurate and efficient models of WECS that can be used to predict both low-frequency transients, e.g. sub-synchronous oscillations (SSO) [3] and high-frequency transients, e.g. behavior during short circuits [4]. The present paper addresses the multi-scale modeling of doubly fed induction generator (DFIG)-based WECS. This type is the most widely used by the wind turbine industry [5].

Simulators of the electromagnetic transients program (EMTP) type [6], [7] make use of nodal analysis and are widely used for studying the behavior of fast transients of DFIG-based WECS [8], [9]. As in all digital simulators, the accuracy of the numerical integration methods across a certain frequency range depends on the time-step size [10]. In the simulation of ac power transmission and distribution systems with the EMTP, an upper limit of the time-step size is given because the ac carrier frequency of either 50 Hz or 60 Hz is represented.

Simulators based on phasor calculus use complex numbers in calculations involving ac voltages and currents. The ac carrier is not represented in phasors. Instead, only the envelopes of ac voltages and currents are tracked. This makes phasor-based simulation efficient for emulating low-frequency transients as for example electromechanical transients. In those cases, time-step sizes can be larger than in the EMTP. WECS models based on phasor calculus were proposed in [11], [12]. If the electromagnetic transients of the electric lines and cables are covered through the application of differential equations in phasor-based simulation, then the modeling is said to involve dynamic phasors [13], [14]. In [15], the model of DFIG-based WECS using dynamic phasors was proposed.

Techniques where the dynamic phasors of nodal voltages are calculated in equations involving a nodal admittance matrix are referred to as shift frequency analysis and modeling [16]–[18]. A further extension is multi-scale modeling that aims at combining the virtues of dynamic phasors and EMTP-type simulation. In frequency-adaptive simulation of transients (FAST) [19], [20], this is achieved by introducing a variable shift frequency and representing all ac voltages and currents through analytic signals, which are complex. Selection of a shift frequency equal to the ac carrier frequency transforms the analytic signals into dynamic phasors with eliminated ac carriers. As opposed to that, a shift frequency of 0 Hz preserves the ac carrier, allowing for the tracking of natural waveforms as in the EMTP. The flexibility of the technique has been proven valuable in [21], [22] for the multi-scale modeling of the transmission line and induction machine.

Manuscript received April 28, 2019; revised September 13, 2019; accepted October 30, 2019. Date of publication December 12, 2019; date of current version February 19, 2020. This work was supported in part by the National Natural Science Foundation of China under Grants 51877115 and 51861135312 and in part by DFG Project AMPSys (STR 1437/3-1). Paper no. TEC-00493-2019. *(Corresponding author: Ying Chen.)*

Y. Xia is with the College of Information and Electrical Engineering, China Agricultural University, Beijing 100083, China (e-mail: xiayuexiayue@163.com).

Y. Chen and Y. Song are with the Department of Electrical Engineering and Applied Electronic Technology, Tsinghua University, Beijing 100084, China (e-mail: chen_ying@tsinghua.edu.cn; songyk13@mails.tsinghua.edu.cn).

K. Strunz is with the Chair of Sustainable Electric Networks and Sources of Energy, Technische Universität Berlin, 10587 Berlin, Germany (e-mail: kai.strunz@tu-berlin.de).

Color versions of one or more of the figures in this article are available online at http://ieeexplore.ieee.org.

Digital Object Identifier 10.1109/TEC.2019.2953893

The multi-scale modeling of WECS was addressed for WECS with synchronous machines in [23]. This paper addresses DFIG-based WECS multi-scale modeling. Besides the well-known differences between those different WECS types, the modeling technique is also further developed in general, resulting in three contributions. Firstly, the WECS is divided into two parts according to the types of waveforms expected. In the part where ac waveforms are not present, the quantities are represented through real signals. The components in this area can be modeled in the same way as they are in EMTP. In the part with ac waveforms, the quantities are represented through analytic signals that support frequency shifting of involved Fourier spectra. The component models are modular, the multi-scale algorithm of FAST is fully encapsulated inside the models. Secondly, to ensure the numerical accuracy and stability of the proposed DFIG-based WECS model, a new interface which links real and analytic signals used in different parts is developed. Furthermore, a method of predicting analytic signals is presented. Accurate and efficient multi-scale simulation across diverse time scales is so supported. Thirdly, a multi-scale voltage-sourced converter (VSC) model with pulse width modulation (PWM) generator is proposed. The average-value and switching-function models of the VSC are selected depending on the types of transients of interest. Test cases are performed to demonstrate the efficiency and accuracy of the proposed model.

In Section II, the key characteristics of analytic signals are reviewed. In Section III, the overall multi-scale model is introduced. The development of the multi-scale model of VSC is described in Section IV. In Section V, the control system model is presented and the interfacing of signals between circuits and controls is addressed. In Section VI, the multi-scale modeling is applied and validated. Conclusions are drawn in Section VII.

II. Analytic Signals and Shift Frequency in Multi-Scale Simulation

A naturally generated signal $s(t)$ is real. The analytic signal $\underline{s}(t)$ can be obtained based on the Hilbert transform [24]:

$$\underline{s}(t) = s(t) + \mathrm{j}\mathcal{H}\left[s(t)\right]. \tag{1}$$

Throughout this paper, the analytic signals are denoted through underscores. As described in [19], frequency shifting can be applied to the analytic signal $\underline{s}(t)$:

$$\mathcal{S}\left[\underline{s}(t)\right] = \underline{s}(t)\mathrm{e}^{-\mathrm{j}2\pi f_{\mathrm{s}} t}, \tag{2}$$

where f_{s} is the shift frequency. The shift frequency plays an important role in the multi-scale simulation. If the shift frequency f_{s} equals zero, the real part of the analytic signal is adopted to track the natural waveform at small time-step sizes as in EMTP. If the shift frequency f_{s} equals the carrier frequency f_{c}, then the complex envelope is obtained. Because $|\mathrm{e}^{-\mathrm{j}2\pi f_{\mathrm{s}} t}| = 1$, the magnitude is not changed through the frequency shifting. The complex envelope is a low-pass signal whose maximum frequency is lower than the one of the original real bandpass signal. As a result, a larger time-step size can be selected when tracking the complex envelope rather than the original bandpass signal. In the multi-scale simulation, both shift frequency and time-step size are adjusted adaptively. Reader may refer to [19] for a detailed description of the selection of shift frequency and time-step size. The method described in [19] is particularly suited for modeling the components in ac power systems where ac carriers and ac waveforms are present.

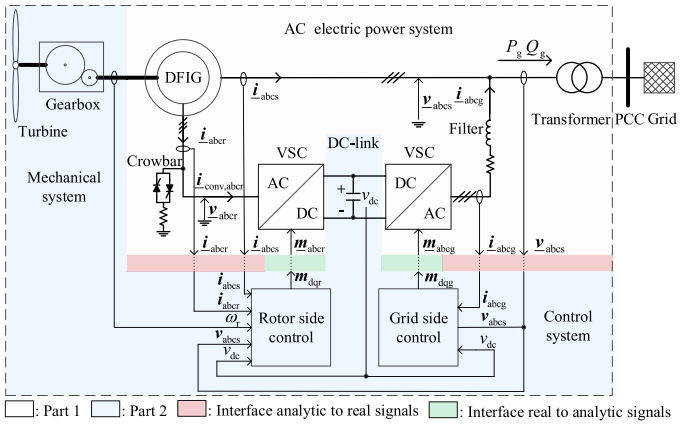

Fig. 1. Multi-scale model of grid-connected DFIG-based WECS.

III. Multi-Scale Modeling of DFIG-Based Wind Energy Conversion System

Fig. 1 shows the structure of a multi-scale model of DFIG-based WECS. The wind turbine is connected to the DFIG through a mechanical shaft system, which consists of a low-speed shaft, a high-speed shaft and a gearbox in between. The DFIG is a wound-rotor induction machine which is fed from both stator and rotor sides. The stator is directly connected to the grid, while the rotor is fed through two back to back VSCs, which are connected by a dc-link circuit [25]. The power conversion from mechanical to electrical power is controlled by the rotor-side converter. The grid-side converter aims to keep the dc-link voltage constant and assure the quality of the output voltage and current in accordance with the standards.

From the viewpoint of the presence of the ac carrier within the system, the DFIG-based WECS shown in Fig. 1 may be divided into two parts:

- Part 1 consists of an ac electric power system which includes modules of two back to back VSCs, DFIG, crowbar, filter, and transformer.
- Part 2 consists of control system, mechanical system, and dc-link circuit.

In part 1, the ac carriers are present within the ac electric power system. The ac quantities are represented through analytic signals. The components in this part are modeled based on FAST. Frequency shifting may be applied. Time-steps are adjusted accordingly to obtain an efficient simulation process. The multi-scale models of DFIG, transformer, and inductor have been proposed in the literature [19], [20], [22]. The focus here is on the multi-scale modeling of VSC.

In part 2, the output variables solved by the simulation program are mainly not modulated by ac carriers. The quantities in part 2, such as rotor speed, change considerably slower than ac quantities in part 1 during electromechanical transients.

TABLE I
QUANTITIES IN MULTI-SCALE MODEL OF DFIG-BASED WECS

Symbol	Signal type	Associated part	Quantity
$\underline{\boldsymbol{v}}_{\mathrm{abcs}}$	analytic	part 1	stator terminal voltages of DFIG
$\underline{\boldsymbol{v}}_{\mathrm{abcr}}$	analytic	part 1	rotor terminal voltages of DFIG
$\underline{\boldsymbol{i}}_{\mathrm{abcs}}$	analytic	part 1	stator currents of DFIG
$\underline{\boldsymbol{i}}_{\mathrm{abcr}}$	analytic	part 1	rotor currents of DFIG
$\underline{\boldsymbol{i}}_{\mathrm{conv,abcr}}$	analytic	part 1	ac-side currents of rotor-side converter
$\underline{\boldsymbol{i}}_{\mathrm{abcg}}$	analytic	part 1	ac-side currents of grid-side converter
$\underline{\boldsymbol{m}}_{\mathrm{abcr}}$	analytic	part 1	modulating signals of rotor-side converter
$\underline{\boldsymbol{m}}_{\mathrm{abcg}}$	analytic	part 1	modulating signals of grid-side converter
P_{g}	real	part 1	active power fed into the grid
Q_{g}	real	part 1	reactive power fed into the grid
$\boldsymbol{v}_{\mathrm{abcs}}$	real	part 2	stator terminal voltages of DFIG
$\boldsymbol{i}_{\mathrm{abcs}}$	real	part 2	stator currents of DFIG
$\boldsymbol{i}_{\mathrm{abcr}}$	real	part 2	rotor currents of DFIG
$\boldsymbol{i}_{\mathrm{abcg}}$	real	part 2	ac-side currents of grid-side converter
$\boldsymbol{m}_{\mathrm{dqr}}$	real	part 2	modulating signals of rotor-side converter
$\boldsymbol{m}_{\mathrm{dqg}}$	real	part 2	modulating signals of grid-side converter
v_{dc}	real	part 2	dc-link voltage
ω_{r}	real	part 2	rotor electrical angular speed

As a result, large time-step sizes may be selected in this part during electromechanical transients without the application of frequency shifting. The components in part 2 are modeled in the same way as they are in EMTP. The dc-link model is described in [23]. A detailed description of the mechanical system model is given [26], [27].

The quantities shown in Fig. 1 are described in Table I. The ac quantities in part 1 are represented through analytic signals denoted by underscores, while the quantities in part 2 are represented through real signals. To maintain compatibility, an interface between two parts is required, as shown by the red and green blocks in Fig. 1. The design of the interface is also the focus of this paper.

IV. MULTI-SCALE MODELING OF VOLTAGE-SOURCED CONVERTER

Among various VSC configurations, the two-level three-phase VSC is the most widely used configuration for WECS applications [5], [28]. A detailed description of the implementation of a VSC model which is suitable for multi-scale transients was, however, not provided before. This section addresses this gap and concentrates on multi-scale modeling of the two-level three-phase VSC.

A. Multi-Scale Voltage-Sourced Converter Model With PWM Generator

The switching function model of the VSC described in [28] is suitable to emulate high-frequency switching transients. However, small time-step sizes are required, resulting in an accordingly large increase in computational cost. An average-value VSC model is an effective alternative to the switching function VSC model when low-frequency phenomena are of main interest [29]. By using the average-value model, a relatively large time-step size can be used, and the computational efficiency is significantly improved.

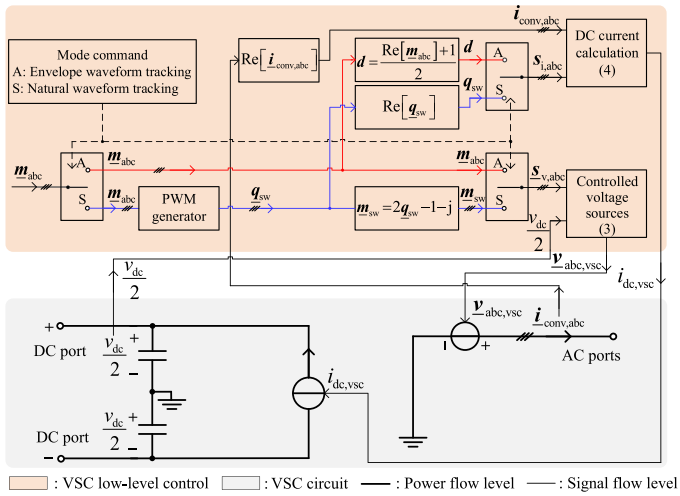

Fig. 2. Multi-scale VSC model including low-level control.

In order to represent multi-scale transients accurately and efficiently, a multi-scale VSC model with PWM generator is proposed. It is modeled by using a combination of both switching function model and an average-complex-value model. Compared with the average-value model used to represent the averages of naturally oscillating ac voltages and currents, the average-complex-value model can, optionally, also track the envelopes of those voltages and currents. The proposed VSC model is presented in Fig. 2. The ac-side and dc-side representation of this model is shown in the gray block. The proposed VSC model appears as a three-phase controlled voltage source at the ac-side and a single-phase controlled current source at the dc-side, consistent with the widely used VSC models in [28]. The controlled voltage source $\underline{\boldsymbol{v}}_{\mathrm{abc,vsc}}$ and controlled current source $i_{\mathrm{dc,vsc}}$ are generated from the VSC low-level control, as shown by the orange block. The ac-side terminal voltages of the VSC are calculated as follows:

$$\underline{\boldsymbol{v}}_{\mathrm{abc,vsc}}(t) = \frac{v_{\mathrm{dc}}(t)}{2}\underline{\boldsymbol{s}}_{\mathrm{v,abc}}(t) \tag{3}$$

where $\underline{\boldsymbol{s}}_{\mathrm{v,abc}}(t)$ are the voltage control signals. The dc-side terminal current of the VSC is given by:

$$i_{\mathrm{dc,vsc}}(t) = \boldsymbol{s}^{\mathrm{T}}_{\mathrm{i,abc}}(t) \cdot \mathrm{Re}\left[\underline{\boldsymbol{i}}_{\mathrm{conv,abc}}(t)\right] \tag{4}$$

with

$$\boldsymbol{s}_{\mathrm{i,abc}}(t) = \left[s_{\mathrm{i,a}}(t), s_{\mathrm{i,b}}(t), s_{\mathrm{i,c}}(t)\right]^{\mathrm{T}}, \tag{5}$$

$$\underline{\boldsymbol{i}}_{\mathrm{conv,abc}}(t) = \left[\underline{i}_{\mathrm{conv,a}}(t), \underline{i}_{\mathrm{conv,b}}(t), \underline{i}_{\mathrm{conv,c}}(t)\right]^{\mathrm{T}}, \tag{6}$$

where $\boldsymbol{s}_{\mathrm{i,abc}}(t)$ are the current control signals, $\underline{\boldsymbol{i}}_{\mathrm{conv,abc}}$ are the VSC ac-side currents, superscript T denotes the transpose of a vector.

As shown in Fig. 2, there are two operation modes for the VSC low-level control: natural waveform tracking and envelope waveform tracking. In natural waveform tracking mode, instantaneous voltages are considered. This mode is suitable for tracking high-frequency electromagnetic transients related to switching. The natural waveform is tracked at small time-step

sizes. The analytic modulating signals $\underline{\boldsymbol{m}}_{\mathrm{abc}}$ are delivered to the PWM generator to generate the switching pulses $\underline{\boldsymbol{q}}_{\mathrm{sw}}$. Here, the switching pulses $\underline{\boldsymbol{q}}_{\mathrm{sw}}$ are modeled as complex signals, consistent with the signals used in the ac electric power system. The used PWM modulation scheme is illustrated in Appendix A. According to the selector shown in Fig. 2, the signals $\underline{\boldsymbol{m}}_{\mathrm{sw}} = 2\underline{\boldsymbol{q}}_{\mathrm{sw}} - 1 - \mathrm{j}$ then determine the voltage control signals $\underline{\boldsymbol{s}}_{\mathrm{v,abc}}$, which are to hold the VSC ac-side voltages within the range of $-\frac{v_{\mathrm{dc}}}{2}$ to $\frac{v_{\mathrm{dc}}}{2}$. The current control signals $\boldsymbol{s}_{\mathrm{i,abc}}$ are obtained by taking the real parts of switching pulses $\underline{\boldsymbol{q}}_{\mathrm{sw}}$. This calculation of control signals corresponding to natural waveform tracking is suitable for the switching function VSC model.

The envelope waveform tracking mode is suitable when low-frequency electromechanical transients are in the focus. The envelope waveforms are tracked with large time-step sizes. The voltage control signals $\underline{\boldsymbol{s}}_{\mathrm{v,abc}}$ are set equal to the modulating signals $\underline{\boldsymbol{m}}_{\mathrm{abc}}$, while the current control signals $\boldsymbol{s}_{\mathrm{i,abc}}$ are set equal to the duty ratios $\boldsymbol{d}$, which are averages of the switching pulses. This mode gives the average-complex-value VSC model. The average-complex-value and switching-function models of the VSC are selected depending on the types of operation modes of interest. Accordingly, the capability to efficiently simulate both electromagnetic and electromechanical transients is made possible.

The most important feature of the multi-scale VSC model is the utilization of full multi-scale representation including all power electronic stages, and low-level power electronic control. Furthermore, the proposed VSC model is modular. This offers considerable programming flexibility. The model can be connected to all available multi-scale models.

The main steps of the implementation of the multi-scale VSC model are detailed in the algorithm of Fig. 3. In step 1, the multi-scale VSC model receives ac-side currents of VSC, dc-link voltage and modulating signals as inputs from the system model solver. In step 2, the operation mode for the VSC low-level control is determined according to the prevailing transients observed. If low-frequency transients are of interest, the envelope waveform tracking mode is selected; otherwise the natural waveform tracking model is selected. In step 3 and step 4, the voltage control signals $\underline{\boldsymbol{s}}_{\mathrm{v,abc}}$ and the current control signals $\boldsymbol{s}_{\mathrm{i,abc}}$ are calculated. Step 5 is performed to calculate the ac-side voltages and dc-side current of VSC. Step 6 is performed to provide information on the voltage sources $\underline{\boldsymbol{v}}_{\mathrm{abc,vsc}}$ and currents source $\underline{\boldsymbol{i}}_{\mathrm{dc,vsc}}$ to the system model solver. The solution of entire system is then obtained. Upon completion, the algorithm of Fig. 3 starts with step 1 again.

B. Network Interfacing of the VSC Model

The interfacing of the rotor-side VSC model and grid-side VSC model with the network model is illustrated in Fig. 4. The controlled current source $i_{\mathrm{dc,rvsc}}$ of the rotor-side VSC model and the controlled current source $i_{\mathrm{dc,gvsc}}$ of the grid-side VSC model are connected to the dc-link circuit. The controlled voltage source $\underline{\boldsymbol{v}}_{\mathrm{abc,rvsc}}$ of the rotor-side VSC model is connected in series with the rotor circuit of the DFIG, while the controlled voltage source $\underline{\boldsymbol{v}}_{\mathrm{abc,gvsc}}$ of the grid-side VSC model is connected

Step 1: Get VSC ac-side currents $\underline{\boldsymbol{i}}_{\mathrm{conv,abc}}(t)$ and dc-link voltage $v_{\mathrm{dc}}(t)$ from the system model solver, get modulating signals $\underline{\boldsymbol{m}}_{\mathrm{abc}}(t)$ from the control system model.

Step 2: Select operation mode for the VSC low-level control according to the prevailing transients observed: if low-frequency transients are of interest, select envelope waveform tracking mode and go to step 3. Else go to step 4.

Step 3: Calculate the voltage control signals and current control signals in envelope tracking mode.

- Step 3.1: Calculate the voltage control signals $\underline{\boldsymbol{s}}_{\mathrm{v,abc}}(t)$: $\underline{\boldsymbol{s}}_{\mathrm{v,abc}}(t) = \underline{\boldsymbol{m}}_{\mathrm{abc}}(t)$.
- Step 3.2: Calculate the duty ratios of modulating signals $\boldsymbol{d}(t)$: $\boldsymbol{d}(t) = \left(\mathrm{Re}\left[\underline{\boldsymbol{m}}_{\mathrm{abc}}(t)\right]+1\right)/2$.
- Step 3.3: Calculate the current control signals $\underline{\boldsymbol{s}}_{\mathrm{i,abc}}(t)$: $\boldsymbol{s}_{\mathrm{i,abc}}(t) = \boldsymbol{d}(t)$, and go to step 5.

Step 4: Calculate the voltage control signals and current control signals in natural waveform tracking mode.

- Step 4.1: Compare the real parts and imaginary parts of modulating signals $\underline{\boldsymbol{m}}_{\mathrm{abc}}(t)$ with a PWM triangular carrier signal, generate switching pluses $\underline{\boldsymbol{q}}_{\mathrm{sw}}(t)$ using the PWM modulation scheme in Appendix A.
- Step 4.2: Calculate the voltage control signals $\underline{\boldsymbol{m}}_{\mathrm{sw}}(t)$: $\underline{\boldsymbol{m}}_{\mathrm{sw}}(t) = 2\underline{\boldsymbol{q}}_{\mathrm{sw}}(t) - 1 - \mathrm{j}$.
- Step 4.3: Calculate the voltage control signals $\underline{\boldsymbol{s}}_{\mathrm{v,abc}}(t)$: $\underline{\boldsymbol{s}}_{\mathrm{v,abc}}(t) = \underline{\boldsymbol{m}}_{\mathrm{sw}}(t)$.
- Step 4.4: Calculate the current control signals: $\boldsymbol{s}_{\mathrm{i,abc}}(t) = \mathrm{Re}\left[\underline{\boldsymbol{q}}_{\mathrm{sw}}\right]$.

Step 5: Calculate ac-side terminal voltages and dc-side terminal current of the VSC.

- Step 5.1: Calculate ac-side terminal voltages $\underline{\boldsymbol{v}}_{\mathrm{abc,vsc}}(t)$ of the VSC using (3).
- Step 5.2: Calculate dc-side terminal current $i_{\mathrm{dc,vsc}}(t)$ of the VSC using (4).

Step 6: Return the voltage source $\underline{\boldsymbol{v}}_{\mathrm{abc,vsc}}(t)$ and current source $i_{\mathrm{dc,vsc}}(t)$ to the system model solver.

Fig. 3. Algorithm of the multi-scale VSC model.

to the filter. The values of $i_{\mathrm{dc,rvsc}}$ and $\underline{\boldsymbol{v}}_{\mathrm{abc,rvsc}}$ are computed as in Section IV-A based on dc-link voltage v_{dc}, modulating signals $\underline{\boldsymbol{m}}_{\mathrm{abcr}}$ and VSC ac-side currents $\underline{\boldsymbol{i}}_{\mathrm{conv,abcr}}$. Similarly, the controlled current source and controlled voltage source of the grid-side VSC model are computed with v_{dc}, $\underline{\boldsymbol{m}}_{\mathrm{abcg}}$ and VSC ac-side currents $\underline{\boldsymbol{i}}_{\mathrm{abcg}}$.

C. Modeling of Rotor-Side VSC During Activation of Crowbar

To avoid the disconnection of the DFIG during grid faults, crowbar protection is widely used [4]. The crowbar consists of a set of thyristors connected in series with a resistor, as shown in Fig. 1. The resistor is used to bypass the excessive rotor current of the DFIG. The crowbar is activated if the dc-link voltage or the rotor current exceed threshold values. When the crowbar is activated, the rotor-side VSC is blocked, the controllers of the rotor-side converter are inactive, and the modulating signals are disabled. The converter ac-side voltage is kept unchanged. The crowbar resistor is connected to the rotor side of the DFIG. The currents flowing through the rotor-side converter are zero when the rotor-side converter is blocked:

$$\underline{\boldsymbol{i}}_{\mathrm{conv,abcr}} = \mathbf{0}\ \mathrm{A}, \tag{7}$$

$$i_{\mathrm{dc,rvsc}} = 0\ \mathrm{A}. \tag{8}$$

At the same time, the DFIG operates as an induction machine. The DFIG model [22] has then to be solved with

$$\underline{\boldsymbol{v}}_{\mathrm{abcr}} = \mathbf{0}\ \mathrm{V}, \tag{9}$$

$$R_{\mathrm{r}}^{'} = R_{\mathrm{r}} + R_{\mathrm{crow}}, \tag{10}$$

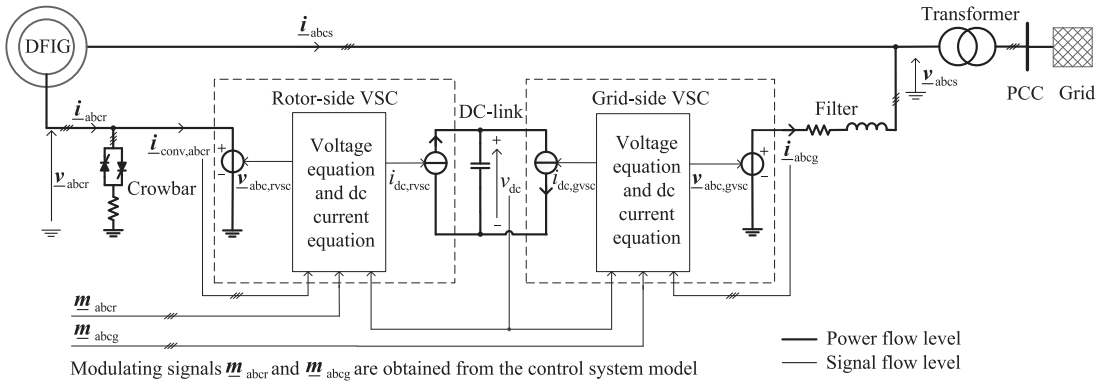

Fig. 4. Network interfacing of rotor-side VSC model and grid-side VSC model.

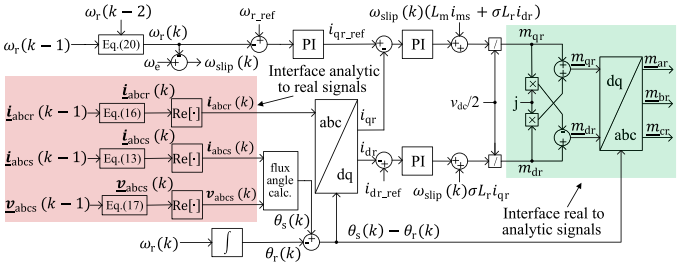

Fig. 5. Model of rotor-side control system with interface between real and analytic signals.

where R_{crow} is the per-phase resistance of the crowbar, $R_{\mathrm{r}}^{'}$ is the per-phase rotor resistance of the DFIG when the crowbar is activated, R_{r} is the per-phase rotor resistance of the DFIG.

V. Modeling and Interfacing of Control System

Operating a DFIG by using vector control is a well-known and widely-employed technique [5]. As illustrated in Fig. 1, the control system model of DFIG-based WECS requires information of ac quantities such as rotor currents, stator currents, and stator voltages. These ac quantities are represented through analytic signals in the ac circuit model. To integrate the analytic signals in the ac circuit model with the real signals in the control system model, an interface is necessary. In the following section, the control system model as well as the interface between the control system model and the ac circuit model are proposed.

A. Modeling and Interfacing of Rotor-Side Control System

The control of the rotor-side converter is based on current vector control with dq decoupling [25]. The control consists of a cascade structure with a fast inner current control loop and a slower outer speed control loop. The model of the rotor-side control system is shown in Fig. 5. The block diagram of flux angle calculation is illustrated in Fig. 18 in Appendix B. The quantities i_{ms} and λ_{s} in Fig. 5 are defined as the equivalent stator magnetizing current and the generator leakage factor, respectively [25]. Those are given in Appendix C for completeness.

As illustrated in Fig. 5, the ac quantities, i.e., $\underline{\boldsymbol{i}}_{\mathrm{abcr}}$, $\underline{\boldsymbol{i}}_{\mathrm{abcs}}$, and $\underline{\boldsymbol{v}}_{\mathrm{abcs}}$ obtained from the ac circuit are used as input signals to the control system model. Because these signals are complex, an interface is required to link the analytic signals in the ac circuit model and real signals in the control system model. The interface is shown by the red and green blocks in Fig. 5. The analytic input signals are converted into real signals by discarding their imaginary parts. To ensure compatibility with the multi-scale VSC model that processes analytic signals, the analytic modulating signals $\underline{m}_{\mathrm{dr}}$ and $\underline{m}_{\mathrm{qr}}$ are constructed by using real modulating signals m_{dr} and m_{qr} as orthogonal imaginary parts as follows:

$$\underline{m}_{\mathrm{dr}} = m_{\mathrm{dr}} - \mathrm{j}m_{\mathrm{qr}}, \tag{11}$$

$$\underline{m}_{\mathrm{qr}} = m_{\mathrm{qr}} + \mathrm{j}m_{\mathrm{dr}}. \tag{12}$$

The method for constructing analytic signals in (11) and (12) has shown to be effective in the multi-scale modeling of the synchronous machine in [30].

The calculations of the control system model and the ac system model are performed by separate solvers. A one time-step delay is introduced inside the control system model. The delay will affect the stability and accuracy of the simulation [31]. Therefore, the input signals to the control system model are predicted to reduce the error of simulation caused by a one time-step delay. The predictions are performed at the interface. The stator currents $\underline{\boldsymbol{i}}_{\mathrm{abcs}}(k)$ at time-step k are predicted as follows:

$$\underline{\boldsymbol{i}}_{\mathrm{abcs}}(k) = \boldsymbol{A}_{\mathrm{i,abcs}}(k)\mathrm{e}^{\mathrm{j}\omega_{\mathrm{e}}\tau(k)}\frac{\underline{\boldsymbol{i}}_{\mathrm{abcs}}(k-1)}{|\underline{\boldsymbol{i}}_{\mathrm{abcs}}(k-1)|}, \tag{13}$$

with

$$\boldsymbol{A}_{\mathrm{i,abcs}}(k) = |\underline{\boldsymbol{i}}_{\mathrm{abcs}}(k-1)| + \zeta\left(|\underline{\boldsymbol{i}}_{\mathrm{abcs}}(k-1)| - |\underline{\boldsymbol{i}}_{\mathrm{abcs}}(k-2)|\right), \tag{14}$$

$$\zeta = \frac{\tau(k)}{\tau(k-1)} \tag{15}$$

where k is the time-step counter; τ is the time-step size; ζ is the ratio of the present to previous time-step sizes; ω_{e} is the ac carrier angular speed; $\boldsymbol{A}_{\mathrm{i,abcs}}$ are the predicted magnitudes of analytic signals $\underline{\boldsymbol{i}}_{\mathrm{abcs}}(k)$ at time-step k. When electromagnetic transients are studied, a very small time-step size is used, the term $\mathrm{e}^{\mathrm{j}\omega_{\mathrm{e}}\tau(k)}$ is nearly equal to 1, and the magnitudes of $\underline{\boldsymbol{i}}_{\mathrm{abcs}}(k-1)$ and $\underline{\boldsymbol{i}}_{\mathrm{abcs}}(k-2)$ between two consecutive steps are nearly

equal. Then, the term $\frac{\boldsymbol{A}_{\mathrm{i,abcs}}(k)}{|\underline{\boldsymbol{i}}_{\mathrm{abcs}}(k-1)|}$ is nearly equal to 1. The stator currents $\underline{\boldsymbol{i}}_{\mathrm{abcs}}(k)$ are predicted by the currents $\underline{\boldsymbol{i}}_{\mathrm{abcs}}(k-1)$ at the previous step.

In the simulation of electromechanical transients, much larger time-step sizes are used. Since the envelope waveforms of analytic electrical quantities change much slower than the natural waveforms during the period of electromechanical transients, a linear extrapolation may be applied to predict the magnitudes of the analytic electrical quantities. The term $\mathrm{e}^{\mathrm{j}\omega_{\mathrm{e}}\tau(k)}$ gives the phase advance of the carrier oscillation over the interval $\tau(k)$. An example is given in Appendix D to show the quality of prediction in (13). Similarly, the rotor currents and stator voltages are predicted as follows:

$$\underline{\boldsymbol{i}}_{\mathrm{abcr}}(k) = \boldsymbol{A}_{\mathrm{i,abcr}}(k)\mathrm{e}^{\mathrm{j}\omega_{\mathrm{slip}}(k)\tau(k)}\frac{\underline{\boldsymbol{i}}_{\mathrm{abcr}}(k-1)}{|\underline{\boldsymbol{i}}_{\mathrm{abcr}}(k-1)|}, \tag{16}$$

$$\underline{\boldsymbol{v}}_{\mathrm{abcs}}(k) = \boldsymbol{A}_{\mathrm{v,abcs}}(k)\mathrm{e}^{\mathrm{j}\omega_{\mathrm{e}}\tau(k)}\frac{\underline{\boldsymbol{v}}_{\mathrm{abcs}}(k-1)}{|\underline{\boldsymbol{v}}_{\mathrm{abcs}}(k-1)|}, \tag{17}$$

with

$$\boldsymbol{A}_{\mathrm{i,abcr}}(k) = |\underline{\boldsymbol{i}}_{\mathrm{abcr}}(k-1)| + \zeta\left(|\underline{\boldsymbol{i}}_{\mathrm{abcr}}(k-1)| - |\underline{\boldsymbol{i}}_{\mathrm{abcr}}(k-2)|\right), \tag{18}$$

$$\boldsymbol{A}_{\mathrm{v,abcs}}(k) = |\underline{\boldsymbol{v}}_{\mathrm{abcs}}(k-1)| + \zeta\left(|\underline{\boldsymbol{v}}_{\mathrm{abcs}}(k-1)| - |\underline{\boldsymbol{v}}_{\mathrm{abcs}}(k-2)|\right), \tag{19}$$

where ω_{slip} is the slip angular speed; $\boldsymbol{A}_{\mathrm{i,abcr}}$ are the predicted magnitudes of rotor currents $\underline{\boldsymbol{i}}_{\mathrm{abcr}}(k)$ at time-step k; $\boldsymbol{A}_{\mathrm{v,abcs}}$ are the predicted magnitudes of stator voltages $\underline{\boldsymbol{v}}_{\mathrm{abcs}}(k)$ at time-step k.

The response of the rotor speed is slower than that of ac quantities due to the inertia of the turbine. Therefore, the rotor speed ω_{r} can be predicted with the linear extrapolation as follows:

$$\omega_{\mathrm{r}}(k) = \omega_{\mathrm{r}}(k-1) + \zeta\left(\omega_{\mathrm{r}}(k-1) - \omega_{\mathrm{r}}(k-2)\right). \tag{20}$$

B. Modeling and Interfacing of Grid-Side Control System

The objective of the grid-side converter is to keep the dc-link voltage at the desired value and ensure operation at a large power factor [5]. A vector control approach is used [25], with a reference frame oriented along the stator voltage vector, resulting in independent control of the active and reactive power flowing between the grid and the grid-side converter. The grid-side converter is current-regulated. The q-axis current i_{qg} is used to control the dc-link voltage, while the d-axis current i_{dg} is used to control the reactive power. Fig. 6 shows the model of the grid-side control system with interface between real and analytic signals. The block diagram of the phase-locked loop (PLL) is illustrated in Fig. 20 in Appendix E.

An interface, which is similar to that of the rotor-side control system model, is designed for the grid-side control system model. The interface is shown by red and green blocks in Fig. 6. The predictions of input signals are essential for enhancement of simulation accuracy. The DFIG stator voltages are predicted using (17). The currents $\underline{\boldsymbol{i}}_{\mathrm{abcg}}(k)$ flowing through the grid-side converter are predicted with analytic signals:

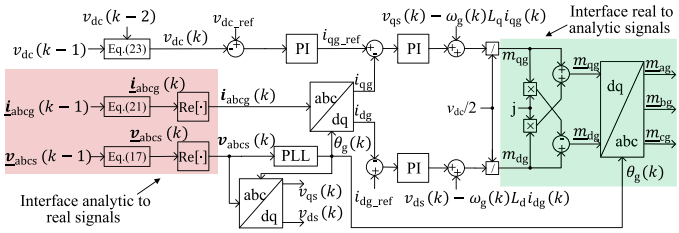

Fig. 6. Model of grid-side control system with interface between real and analytic signals.

$$\underline{\boldsymbol{i}}_{\mathrm{abcg}}(k) = \boldsymbol{A}_{\mathrm{i,abcg}}(k)\mathrm{e}^{\mathrm{j}\omega_{\mathrm{e}}\tau(k)}\frac{\underline{\boldsymbol{i}}_{\mathrm{abcg}}(k-1)}{|\underline{\boldsymbol{i}}_{\mathrm{abcg}}(k-1)|}, \tag{21}$$

with

$$\boldsymbol{A}_{\mathrm{i,abcg}}(k) = |\underline{\boldsymbol{i}}_{\mathrm{abcg}}(k-1)| + \zeta\left(|\underline{\boldsymbol{i}}_{\mathrm{abcg}}(k-1)| - |\underline{\boldsymbol{i}}_{\mathrm{abcg}}(k-2)|\right), \tag{22}$$

where $\boldsymbol{A}_{\mathrm{i,abcg}}$ are the predicted magnitudes of analytic signals $\underline{\boldsymbol{i}}_{\mathrm{abcg}}(k)$ at time-step k.

The dc-link voltage $v_{\mathrm{dc}}(k)$ is predicted using linear extrapolation:

$$v_{\mathrm{dc}}(k) = v_{\mathrm{dc}}(k-1) + \zeta\left(v_{\mathrm{dc}}(k-1) - v_{\mathrm{dc}}(k-2)\right). \tag{23}$$

VI. Validation and Test Simulation

In order to validate the proposed multi-scale model of DFIG-based WECS, three tests are performed. In Section VI-A, the system behavior is simulated with a wind sequence having an average speed of about 9 m/s. It is validated that a large time-step size can be selected for the proposed multi-scale model only when envelope waveforms are of interest. In Section VI-B, a case study involving a three-phase-to-ground fault and covering diverse transients is carried out. It is demonstrated how the proposed model supports accurate and efficient multi-scale simulation within one and the same study. In Section VI-C, it is shown that the proposed model is effective in simulating unbalanced fault.

A. Efficient Simulation of DFIG-Based WECS Under Wind Fluctuation

A wind model as defined in [5] is applied to a 1.5 MW DFIG-based WECS. The test system is shown in Fig. 1. The system parameters are given in Appendix F. The system operates under a wind speed varying around an average of 9 m/s. In this case, only electromechanical transients are observed. To allow for efficient simulation of electromechanical transients, the average-value VSC model is adopted, and a large time-step of 8 ms and a shift frequency of 60 Hz are chosen for the proposed multi-scale model. For the purpose of comparison, the system is also modeled using PSCAD/EMTDC. The average-value VSC model is used in EMTDC. In order to obtain an accurate solution, the model of EMTDC is solved at a small time-step size of 10 μs.

The wind speed series is depicted in Fig. 7. The active power fed into the grid and the generator angular speed are shown

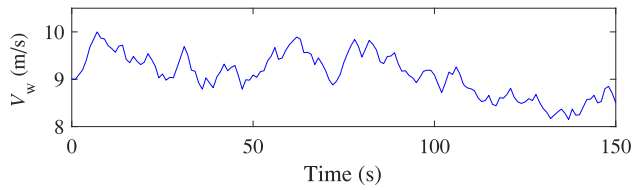

Fig. 7. Time series of wind speed over 150 s.

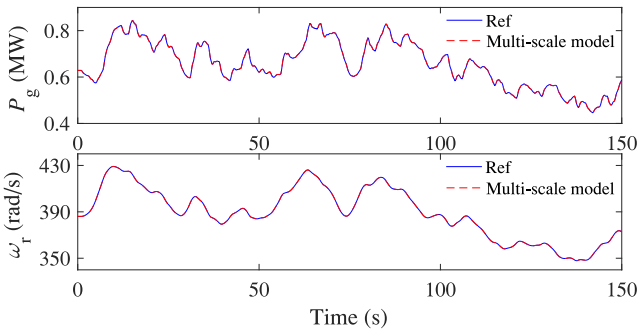

Fig. 8. Simulation results; (a) active power; solid: reference solutions obtained from the model of EMTDC, dashed: solutions for the proposed model; (b) generator angular speed; solid: reference solutions obtained from the model of EMTDC, dashed: solutions for the proposed model.

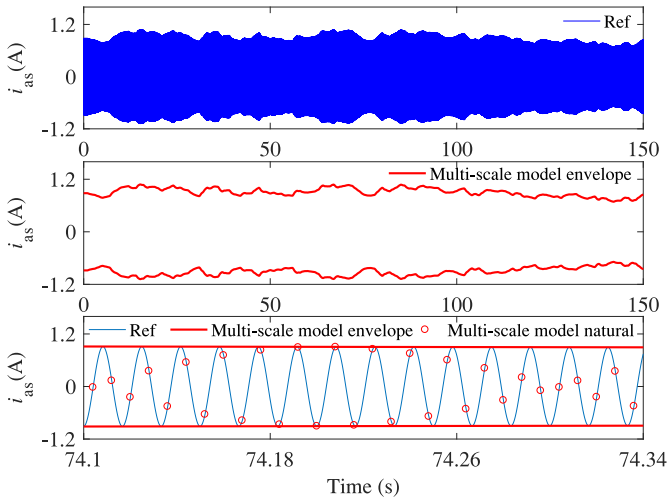

Fig. 9. Phase a stator current i_{as}; (a) natural waveforms of the reference solution in EMTDC; (b) envelope waveforms processed by the multi-scale model; (c) zoomed-in view of i_{as}, solid light: natural waveforms of the reference solution; solid bold: envelope waveforms processed by the multi-scale model; circle: natural waveforms processed by the multi-scale model.

in Fig. 8. The results obtained with the proposed multi-scale model closely match the reference solutions. Fig. 9 shows the stator current i_{as} of the DFIG. The model of EMTDC processes instantaneous signals to track natural waveforms, as depicted in Fig. 9(a), while the proposed model processes phasor signals to track envelope waveforms, as depicted in Fig. 9(b). To examine the accuracy of envelope waveforms processed by the multi-scale model, the instantaneous values of the stator current i_{as} are obtained using the real parts of the analytic signals according to (1). The natural waveforms processed by the multi-scale

TABLE II
SIMULATION ACCURACIES OF THE PROPOSED MODEL

Quantities	2-norm errors (%)
active power P_g	0.05
rotor angular speed ω_r	0.01
stator current i_{as}	0.91

TABLE III
SETTING OF SHIFT FREQUENCY f_s, TIME-STEP SIZE τ, AND VSC MODEL IN MULTI-SCALE SIMULATION

Time (s)	Stages	f_s (Hz)	τ (s)	VSC model
0.00-0.25	steady state	60	8e-3	average-complex-value
0.25-0.85	electromagnetic transients	0	10e-6	switching function
0.85-2.00	electromechanical transients	60	8e-3	average-complex-value

model are represented using circles in Fig. 9(c). It can be seen that there is no visible difference between the results obtained with the multi-scale model and the model of EMTDC.

In order to further investigate the accuracy of the proposed model, the 2-norm cumulative relative errors are used [32]:

$$\varepsilon(x) = \frac{\|x_{\text{ref}} - x\|_2}{\|x_{\text{ref}}\|_2} \times 100\%, \tag{24}$$

where x represents the result obtained with the proposed model, x_{ref} represents the reference solution obtained with the model of EMTDC, and $\| x \|_2$ represents 2-norm of x. The 2-norm errors of active power P_g, rotor angular speed ω_r and stator current i_{as} are given in Table II. Even with a very large time-step size of 8 ms, the error of the proposed model in the stator current i_{as} is less than 1%. A high degree of accuracy of the proposed model is confirmed.

The computational efficiency is compared with that of an EMTP-type implementation of equal structure. Analytic signals are used in the proposed multi-scale model, while real signals are used for the EMTP-type implementation. The processing of analytic rather than real signals increases the computational cost by a factor of 1.4 per time-step. For the electromechanical transients in above example, the proposed model may use a large time-step size of 8 ms. To achieve similar accuracy, a small time-step size of 10 μs is required for the EMTP-type implementation. Taking into account that analytic signals are processed, the speed-up of computation is at a factor of about $(8\text{ ms})/(10\ \mu\text{s})/1.4 = 571$.

B. Multi-Scale Simulation of DFIG-Based WECS During a Balanced Fault

To further validate the proposed model, a simulation covering diverse transients as shown in Table III is performed in the test system of Fig. 1. Initially, the system operates in the steady state. The wind speed is maintained at rated speed of 12 m/s. A three-phase-to-ground fault occurs at the point of common coupling (PCC) at $t = 0.25$ s. Such a fault triggers electromagnetic transients. The fault is cleared at $t = 0.4$ s. After further 0.45 s, the test case is dominated by electromechanical transients. For the purpose of comparison, the system is also modeled using

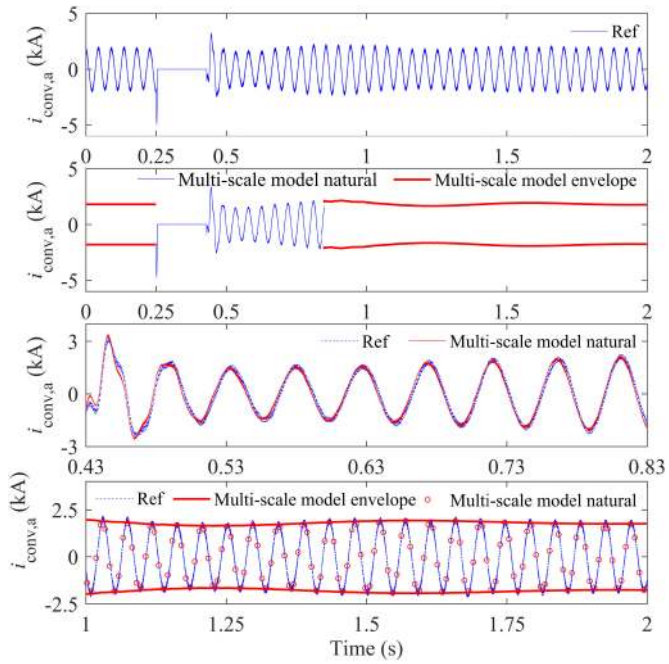

Fig. 10. Phase a current $i_{\mathrm{conv,a}}$ of rotor-side converter; (a) natural waveform of the reference solution in EMTDC; (b) natural and envelope waveforms in the multi-scale simulation; solid light: natural waveform; solid bold: envelope; (c) zoomed-in view of $i_{\mathrm{conv,a}}$ during electromagnetic transients, dashed: natural waveform of the reference solution in EMTDC; solid: natural waveforms in the multi-scale simulation; (d) zoomed-in view of $i_{\mathrm{conv,a}}$ during electromechanical transients, solid light: natural waveform of the reference solution; solid bold: envelope waveforms in the multi-scale simulation; circle: natural waveforms in the multi-scale simulation.

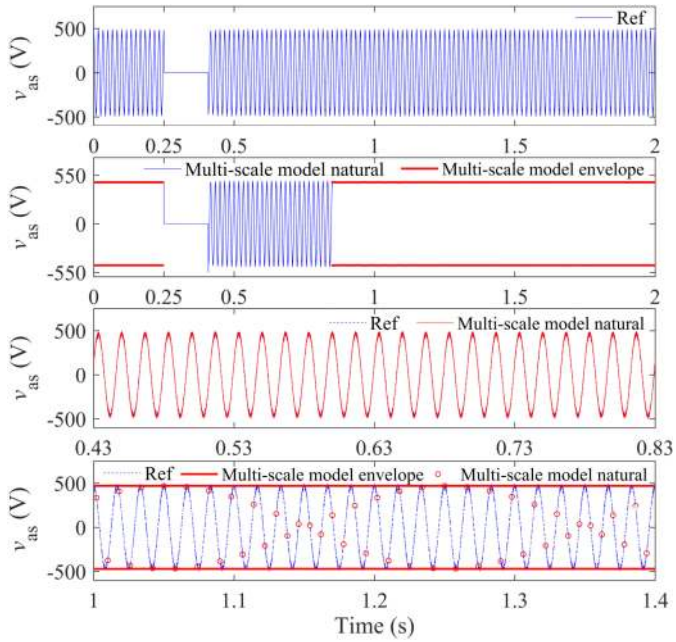

Fig. 11. Phase a stator voltage v_{as} of DFIG; (a) natural waveform of the reference solution in EMTDC; (b) natural and envelope waveforms in the multi-scale simulation; solid light: natural waveform; solid bold: envelope; (c) zoomed-in view of v_{as} during electromagnetic transients, dashed: natural waveform of the reference solution in EMTDC; solid: natural waveforms in the multi-scale simulation; (d) zoomed-in view of v_{as} during electromechanical transients, solid light: natural waveform of the reference solution; solid bold: envelope waveforms in the multi-scale simulation; circle: natural waveforms in the multi-scale simulation.

EMTDC. Due to the presence of the high-frequency transients, the switching function VSC model is used in EMTDC throughout the simulation. To obtain accurate simulation results, the time-step size is set to 10 μs in EMTDC. The current flowing through the rotor-side converter is depicted in Fig. 10. The stator voltage of DFIG in phase a is depicted in Fig. 11. The rotor electrical angular speed is depicted in Fig. 12. The active power and reactive power fed into the grid are depicted in Fig. 13. It is clear that the results obtained with the multi-scale model and EMTDC match closely.

At the beginning of the simulation, the system is running in the steady state. The generated active power is about 1.5 MW. As shown in Table III, the proposed multi-scale model offers a large time-step simulation to show the behavior of the system in steady state, and the average-complex-value model of the VSC is chosen. Envelope waveforms are tracked as shown in Fig. 10(b) and Fig. 11(b). At $t = 0.25$ s, a three-phase-to-ground fault occurs at the terminals of the transformer. To avoid over-current flowing through the rotor-side converter, the rotor-side converter is blocked and the crowbar circuit is activated. The DFIG rotor currents flow through the crowbar instead of the rotor-side converter. The generator operates as an induction machine. The fault triggers electromagnetic transients to appear. Then, it is interesting to give a detailed simulation. The switching function model of the VSC is chosen. The time-step size is set to 10 μs, and the shift frequency is set to zero. The natural

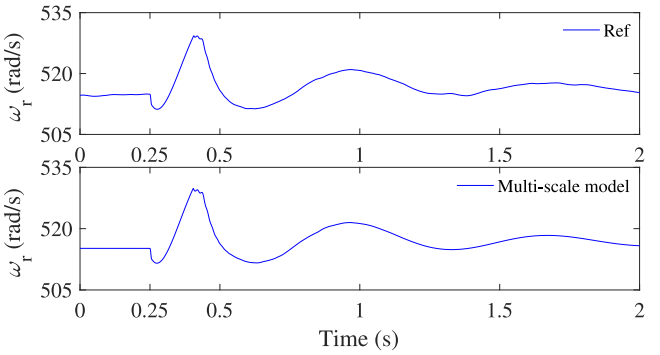

Fig. 12. Rotor electrical angular speed ω_{r}; (a) reference solution in EMTDC; (b) results obtained with the proposed model.

TABLE IV
2-NORM ERRORS OF THE ROTOR ELECTRICAL ANGULAR SPEED

Time (s)	Stages	2-norm errors of ω_{r} (%)
0.25-0.85	electromagnetic transients	0.10
0.85-2.00	electromechanical transients	0.09

waveforms are tracked. At $t = 0.4$ s, the fault is cleared. The restart procedure of the rotor-side converter is delayed after the fault clearance to avoid over-current in the rotor circuit [33]. At $t = 0.43$ s, the rotor currents decay to a safe value, the crowbar is removed. The rotor-side converter resumes its operation. The

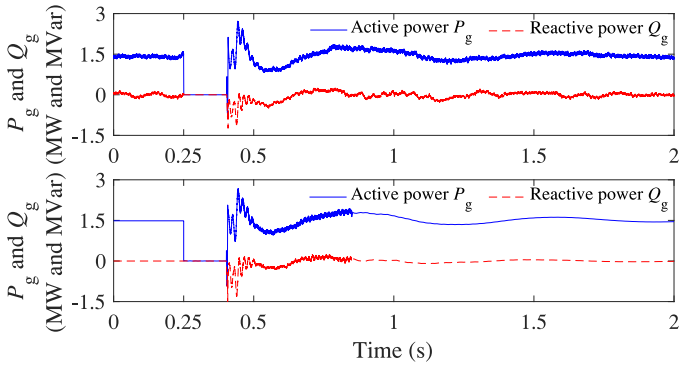

Fig. 13. Active power P_g and reactive power Q_g; (a) reference solution in EMTDC, solid: active power, dashed: reactive power; (b) results obtained with the proposed model, solid: active power, dashed: reactive power.

active power and reactive power can be controlled. In this period, electromagnetic transients still exist in the system. The tracking of natural waveforms continues. At about $t = 0.85$ s, the electromagnetic transients due to the clearance of the fault have sufficiently damped out. Remaining electromechanical transients are emulated with envelope tracking at $\tau = 8$ ms and $f_s = 60$ Hz. The shift frequency and the time-step size are being set according to the rules discussed in Section II or in greater detail in [19].

The 2-norm errors of rotor electrical angular speed ω_r are given in Table II. During electromagnetic transients stage, the proposed multi-scale model uses a time-step size of 10 μs, the 2-norm error is 0.1%. During electromechanical transients stage, a much larger time-step size of 8 ms is used for the multi-scale model, the 2-norm error is 0.09%. Of interest is also a comparison of the computational efficiency. In the multi-scale simulation, the analytic signals are used, the real signals are used for the EMTP-type implementation. During the stage of electromagnetic transients, a very small time-step size of 10 μs is required by both implementations. The processing of analytic rather than real signals leads to a factor of about 1.41 in increased computational cost. During the stage of electromechanical transients, the multi-scale model uses a much larger time-step size of 8 ms. The computational speed with the multi-scale representation is $(8\text{ ms})/(10\ \mu\text{s})/1.41 = 567$ times faster than that with the EMTP-type implementation.

C. Multi-Scale Simulation of DFIG-Based WECS During an Unbalanced Fault

In this section, an unbalanced fault is considered. The DFIG-based WECS initially operate in the steady state. Phase a is shorted to ground at PCC at $t = 0.25$ s. After five cycles, the fault is cleared. As in Section VI-B, multi-scale simulation is also applied in this case. For the purpose of comparison, the fault is also simulated in EMTDC. In EMTDC, the switching function VSC model is adopted and the time-step size is set to 10 μs. The stator currents of DFIG in phase a and phase c are shown in Fig. 14 and Fig. 15, respectively. The electromagnetic torque of DFIG is shown in Fig. 16. From Fig. 14, Fig. 15 and Fig. 16, it can

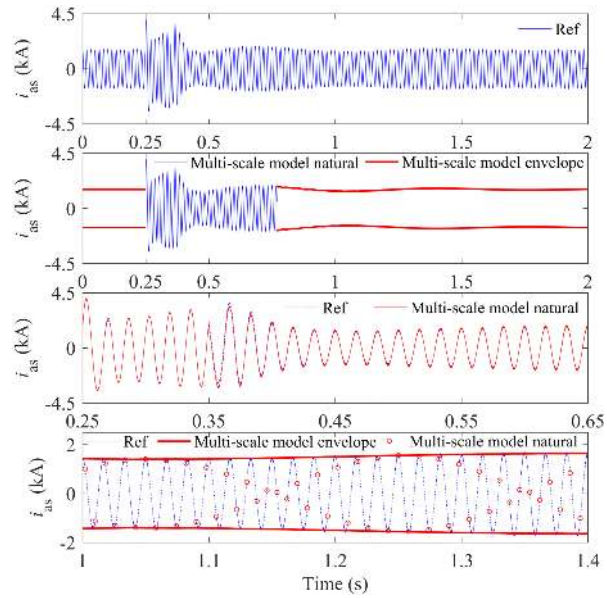

Fig. 14. Phase a stator current i_{as} of DFIG; (a) natural waveform of the reference solution in EMTDC; (b) natural and envelope waveforms in the multi-scale simulation; solid light: natural waveform; solid bold: envelope; (c) zoomed-in view of i_{as} during electromagnetic transients, dashed: natural waveform of the reference solution in EMTDC; solid: natural waveforms in the multi-scale simulation; (d) zoomed-in view of i_{as} during electromechanical transients, solid light: natural waveform of the reference solution; solid bold: envelope waveforms in the multi-scale simulation; circle: natural waveforms in the multi-scale simulation.

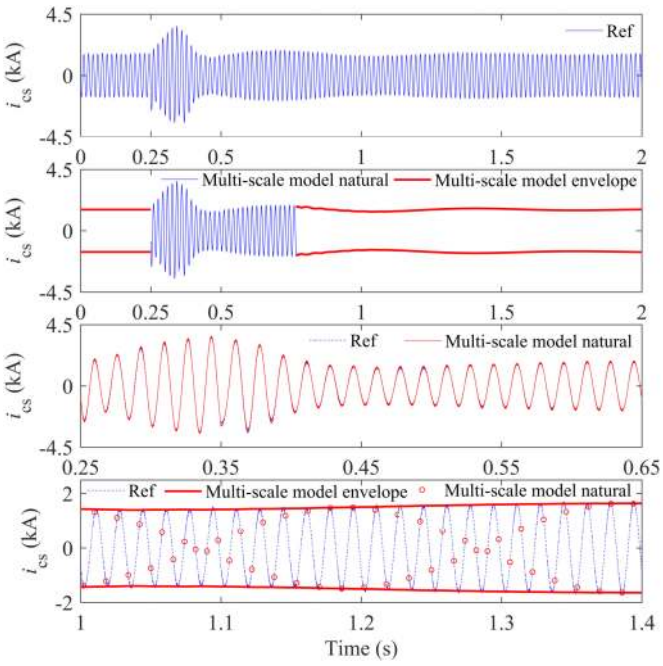

Fig. 15. Phase c stator current i_{cs} of DFIG; (a) natural waveform of the reference solution in EMTDC; (b) natural and envelope waveforms in the multi-scale simulation; solid light: natural waveform; solid bold: envelope; (c) zoomed-in view of i_{cs} during electromagnetic transients, dashed: natural waveform of the reference solution in EMTDC; solid: natural waveforms in the multi-scale simulation; (d) zoomed-in view of i_{cs} during electromechanical transients, solid light: natural waveform of the reference solution; solid bold: envelope waveforms in the multi-scale simulation; circle: natural waveforms in the multi-scale simulation.

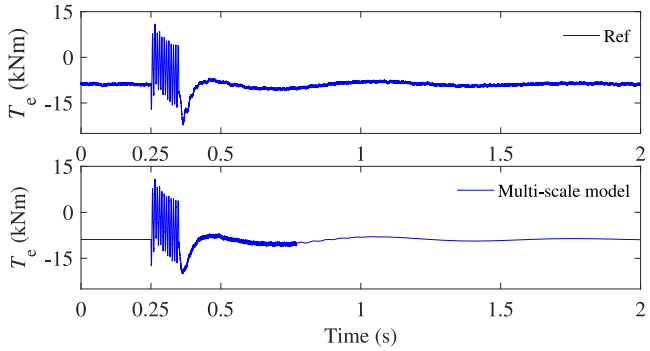

Fig. 16. Electromagnetic torque T_e; (a) reference solution in EMTDC; (b) results obtained with the proposed model.

be seen that no differences between the multi-scale simulation and the corresponding EMTDC simulation are visible.

Initially, the WECS is in the steady-state. The time-step size is set to 8 ms, the shift frequency is set to 60 Hz, and the average-complex-value model of VSC is adopted at the beginning of the simulation. At $t = 0.25$ s, electromagnetic transients are triggered as a consequence of the single-phase-to-ground fault. To get more details, the switching function model of the VSC is chosen. Natural waveforms are tracked at $\tau = 10$ μs and $f_s = 0$ Hz. At about $t = 0.77$ s, the electromagnetic transients have largely damped out. The envelope tracking resumes at $\tau = 8$ ms and $f_s = 60$ Hz, and the average-complex-value model of VSC is adopted.

VII. Conclusion

A multi-scale model for simulation of a DFIG-based WECS was developed, implemented, and validated. The proposed model serves as a general model capable of simulating both electromagnetic and electromechanical transients by tracking natural and envelope waveforms within one and the same simulation run.

The proposed model is distinguished by three contributions. First, the WECS is divided into two parts in which different modeling techniques are used. In the part where ac waveforms are present, the quantities are represented with analytic signals and the components are modeled using a modular approach, thus the multi-scale simulation algorithm of FAST is fully encapsulated inside the model. In the part where ac waveforms are not present, the quantities are represented through real signals and the components are modeled in the same way as they are modeled in EMTP. Second, an interface is designed to link the real and analytic signals between the two parts. A new mathematical prediction of analytic signals is proposed at the interface. Third, a multi-scale VSC model with PWM generator is proposed. When slow transients are of interest, an average-complex-value VSC model is used, and a large time-step size is chosen to ensure a high computational efficiency. Since the average-complex-value model processes analytic signals, it can be used to track envelope waveforms or instantaneous values of natural waveforms. In the simulation of fast transients,

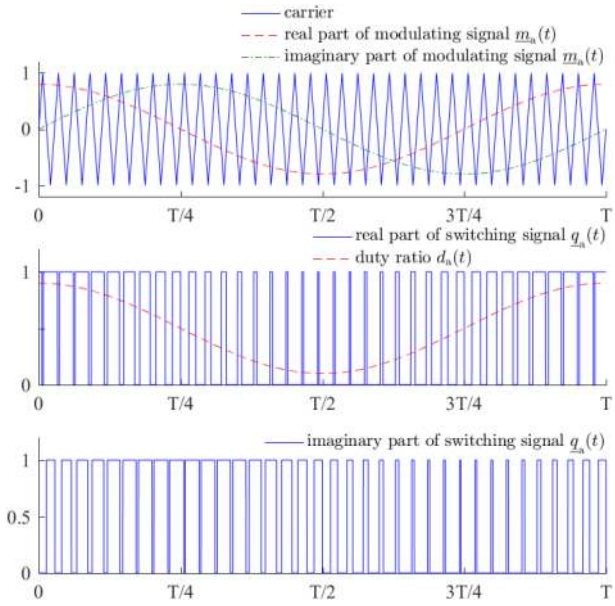

Fig. 17. Relations of modulation, switching, and duty ratio.

a switching-function VSC model is selected, and a small time-step size is used to provide a detailed representation. Accurate and efficient simulation is made possible by choosing between these two types of VSC models. Test studies demonstrated that the proposed model provides accurate and efficient multi-scale simulation.

Appendix

A. Generation of Switching Pulses in Multi-Scale Simulation

The ac-side model of the VSC is directly connected to an ac network model. Therefore, the ac-side terminal voltages of the VSC are represented using analytic signals. Accordingly, a PWM modulation scheme is modeled to provide complex switching pulses as illustrated in Fig. 17. The switching pulses are used to calculate the ac-side terminal voltages of the VSC. The real parts and imaginary parts of the modulating signals $\underline{m}_a(t)$ are compared with a PWM triangular carrier signal. The latter is assumed to have peaks of -1 and $+1$, and real parts and imaginary parts of $\underline{m}_a(t)$ also lie within that range. The real parts and imaginary parts of the complex switching pulses $\underline{q}_a(t)$ are obtained from the comparison. The duty ratio $d_a(t)$ is the average of the switching pulses $q_a(t)$. The duty ratio $d_a(t)$ and modulating signal $\underline{m}_a(t)$ are related by

$$d_a(t) = \frac{\mathrm{Re}\left[\underline{m}_a(t)\right] + 1}{2}. \tag{25}$$

B. Stator Flux Angle Calculation

The stator flux angle may be calculated as follows [25]:

$$\theta_s(t) = \tan^{-1}\frac{\lambda_{\beta s}(t)}{\lambda_{\alpha s}(t)}, \tag{26}$$

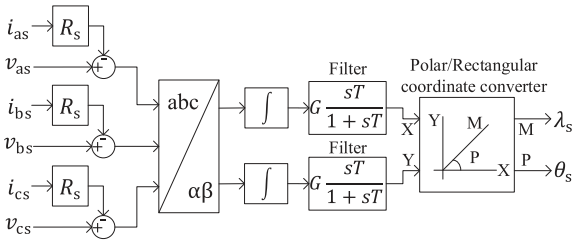

Fig. 18. Block diagram of stator flux angle calculation.

with

$$\lambda_{\alpha s}(t) = \int \left(v_{\alpha s}(t) - R_s i_{\alpha s}(t)\right) \mathrm{d}t, \tag{27}$$

$$\lambda_{\beta s}(t) = \int \left(v_{\beta s}(t) - R_s i_{\beta s}(t)\right) \mathrm{d}t, \tag{28}$$

where $\theta_s(t)$ is the stator flux vector position, R_s is the DFIG stator resistance, $i_{\alpha s}(t)$ and $i_{\beta s}(t)$ are the DFIG stator currents in $\alpha\beta$ reference frame, $v_{\alpha s}(t)$ and $v_{\beta s}(t)$ are the DFIG stator voltages in $\alpha\beta$ reference frame. Fig. 18 illustrates the block diagram of flux angle calculation. To eliminate DC offsets, passband filters are used to solve the integral in (27) and (28).

C. Coefficients in Control System Model

The quantity i_{ms} in Fig. 5 is defined as the equivalent stator magnetizing current. Under stator flux orientation, i_{ms} is given by [25]:

$$i_{ms} = \frac{\lambda_s}{L_m}, \tag{29}$$

where λ_s denotes the stator flux, L_m denotes the DFIG magnetizing inductance. The quantity σ denotes the generator leakage factor, and it is defined as:

$$\sigma = 1 - \frac{L_m^2}{L_s L_r}, \tag{30}$$

where L_s and L_r denote the stator and rotor inductances, respectively.

D. Prediction of Analytic Signals

Let an ac source voltage be described by the following excitation function:

$$v_e(t) = \hat{V}_e(t)\sin\left(2\pi f_c t\right), \tag{31}$$

with

$$\hat{V}_e(t) = \sin\left(2\pi f_m t\right), \quad f_c = 60\ \mathrm{Hz}\ f_m = 1\ \mathrm{Hz}, \tag{32}$$

where $\hat{V}_e(t)$ represents the amplitude of the source voltage.

Through the Hilbert transform, an analytic signal is created based on (1):

$$\underline{v}_e(t) = \hat{V}_e(t)\mathrm{e}^{\left(\mathrm{j}2\pi f_c t - \mathrm{j}\frac{\pi}{2}\right)}. \tag{33}$$

It is assumed that the voltage v_e and $\hat{V}_e$ at $t-\tau$ are known and that the voltage v_e at t is to be found.

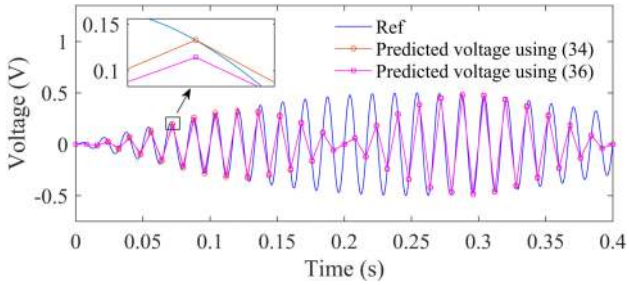

Fig. 19. Predictions of voltage $v_e(t)$ using a time-step size of 8 ms.

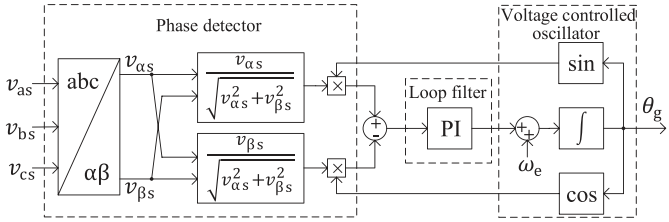

Fig. 20. Block diagram of PLL.

TABLE V
WIND TURBINE AND DRIVE TRAIN PARAMETERS

Symbol	Quantity	Value
P_{tur}	rated power	1.5 MW
V_w	rated wind speed	12 m/s
$C_{P,opt}$	maximum power coefficient	0.374
λ_{opt}	optimal tip speed ratio	7
β	pitch angle	5°
r	rotor radius	35.25 m
H_t	inertia constant of turbine	4.32 s
n_g	gear box ratio	72
K_{ls}	low speed shaft stiffness	0.64 p.u.
D_{ls}	low speed shaft damping coefficient	1.5 p.u.

Prediction of v_e based on (13) gives:

$$\tilde{\underline{v}}_e(t) = \boldsymbol{A}_{ve}(t)\mathrm{e}^{\mathrm{j}2\pi f_c \tau}\frac{\underline{v}_e(t-\tau)}{\hat{V}_e(t-\tau)} \tag{34}$$

with

$$\boldsymbol{A}_{ve}(t) = \hat{V}_e(t-\tau) + \zeta\left(\hat{V}_e(t-\tau) - \hat{V}_e(t-2\tau)\right). \tag{35}$$

The results of the predictions are shown in Fig. 19 for $\tau = 8$ ms. For comparison, the voltage source v_e is also predicted using the method in [22], [23]:

$$\tilde{\underline{v}}_e(t) = \mathrm{e}^{\mathrm{j}2\pi f_c \tau}\underline{v}_e(t-\tau). \tag{36}$$

As shown in Fig. 19, the results obtained with (34) are more accurate than that obtained with (36).

E. Phase-Locked Loop (PLL)

Fig. 20 illustrates the PLL block diagram. The PLL [34] consists of a phase detector (PD), a loop filter (LF) and a voltage controlled oscillator (VCO).

TABLE VI
DFIG PARAMETERS

Symbol	Quantity	Value
p	number of pole pairs	3
$V_{\rm n}$	rated voltage(line to line)	575 V
$f_{\rm n}$	rated frequency	60 Hz
$R_{\rm s}$	stator resistance	0.023 p.u.
$R_{\rm r}$	rotor resistance	0.016 p.u.
$L_{\rm s}$	stator inductance	0.18 p.u.
$L_{\rm r}$	rotor inductance	0.16 p.u.
$L_{\rm m}$	mutual inductance	2.9 p.u.
$H_{\rm g}$	inertia constant of generator	0.685 s

TABLE VII
CONVERTER, CROWBAR, FILTER, AND TRANSFORMER PARAMETERS

Symbol	Quantity	Value
$f_{\rm rvsc}$	rotor-side VSC switching frequency	1800 Hz
$f_{\rm gvsc}$	grid-side VSC switching frequency	2700 Hz
$C_{\rm dc}$	dc-link capacitance	60 mF
$v_{\rm dc}$	dc-link voltage	1150 V
$R_{\rm crow}$	crowbar resistance	0.64 p.u.
$R_{\rm f}$	filter resistance	0.003 p.u.
$L_{\rm f}$	filter inductance	0.3 p.u.
$L_{\rm t}$	transformer inductance	0.05 p.u.

TABLE VIII
GRID PARAMETERS

Symbol	Quantity	Value
$V_{\rm g}$	grid voltage	25 kV
$f_{\rm g}$	grid frequency	60 Hz
$R_{\rm g}$	grid resistance	0.532 Ω
$L_{\rm g}$	grid inductance	0.02 H

F. Parameters of Test Systems

Table V, Table VI, and Table VII summarize the parameters of the reference WECS. The grid parameters are given in Table VIII. The parameters are obtained from [23], [35], [36].

REFERENCES

[1] V. Fthenakis and H. C. Kim, "Land use and electricity generation: A life-cycle analysis," *Renew. Sustain. Energy Rev.*, vol. 13, no. 6, pp. 1465–1474, Aug. 2009.

[2] G. W. E. Council, "Global wind report 2015," [Online]. Available: http://www.gwec.net.

[3] W. Du, Y. Wang, H. Wang, and Q. Fu, "Concept of modal repulsion for examining the sub-synchronous oscillations in power systems," *IEEE Trans. Power Syst.*, vol. 34, no. 1, pp. 518–526, Jan. 2019.

[4] I. Erlich, J. Kretschmann, J. Fortmann, S. Mueller-Engelhardt, and H. Wrede, "Modeling of wind turbines based on doubly-fed induction generators for power system stability studies," *IEEE Trans. Power Syst.*, vol. 22, no. 3, pp. 909–919, Aug. 2007.

[5] I. Munteanu, A. I. Bratcu, N. A. Cutululis, and E. Ceanga, *Optimal Control of Wind Energy Systems: Towards a Global Approach*. Berlin, Germany: Springer, 2008.

[6] H. W. Dommel, "Digital computer solution of electromagnetic transients in single- and multiphase networks," *IEEE Trans. Power App. Syst.*, vol. PAS-88, no. 4, pp. 388–399, Apr. 1969.

[7] N. Watson and J. Arrillaga, *Power Systems Electromagnetic Transients Simulation*. London, U.K.: Institution of Electrical Engineers, 2003.

[8] L. Xu and Y. Wang, "Dynamic modeling and control of DFIG-based wind turbines under unbalanced network conditions," *IEEE Trans. Power Syst.*, vol. 22, no. 1, pp. 314–323, Feb. 2007.

[9] S. K. Salman and A. L. J. Teo, "Windmill modeling consideration and factors influencing the stability of a grid-connected wind power-based embedded generator," *IEEE Trans. Power Syst.*, vol. 18, no. 2, pp. 793–802, May 2003.

[10] K. Strunz, "Position-dependent control of numerical integration in circuit simulation," *IEEE Trans. Circuits Syst. II, Express Briefs*, vol. 51, no. 10, pp. 561–565, Oct. 2004.

[11] J. G. Slootweg, H. Polinder, and W. L. Kling, "Representing wind turbine electrical generating systems in fundamental frequency simulations," *IEEE Trans. Energy Convers.*, vol. 18, no. 4, pp. 516–524, Dec. 2003.

[12] M. Rosyadi, A. Umemura, R. Takahashi, J. Tamura, S. Kondo, and K. Ide, "Development of phasor type model of PMSG based wind farm for dynamic simulation analysis," in *Proc. IEEE Eindhoven PowerTech*, Eindhoven, The Netherlands, 2015.

[13] T. Yang, S. Bozhko, J. M. Le-Peuvedic, G. Asher, and C. I. Hill, "Dynamic phasor modeling of multi-generator variable frequency electrical power systems," *IEEE Trans. Power Syst.*, vol. 31, no. 1, pp. 563–571, Jan. 2016.

[14] Y. Huang, L. Dong, S. Ebrahimi, N. Amiri, and J. Jatskevich, "Dynamic phasor modeling of line-commutated rectifiers with harmonics using analytical and parametric approaches," *IEEE Trans. Energy Convers.*, vol. 32, no. 2, pp. 534–547, Jun. 2017.

[15] S. Chandrasekar and R. Gokaraju, "Dynamic phasor modeling of type 3 DFIG wind generators (including SSCI phenomenon) for short-circuit calculations," *IEEE Trans. Power Del.*, vol. 30, no. 2, pp. 887–897, Apr. 2015.

[16] P. Zhang, J. R. Martí, and H. W. Dommel, "Shifted-frequency analysis for EMTP simulation of power-system dynamics," *IEEE Trans. Circuits Syst. I*, vol. 57, no. 9, pp. 2564–2574, Sep. 2010.

[17] D. Shu, V. Dinavahi, X. Xie, and Q. Jiang, "Shifted frequency modeling of hybrid modular multilevel converters for simulation of MTDC grid," *IEEE Trans. Power Del.*, vol. 33, no. 3, pp. 1288–1298, Jun. 2018.

[18] Y. Huang, M. Chapariha, F. Therrien, J. Jatskevich, and J. R. Martí, "A constant-parameter voltage-behind-reactance synchronous machine model based on shifted-frequency analysis," *IEEE Trans. Energy Convers.*, vol. 30, no. 2, pp. 761–771, Jun. 2015.

[19] K. Strunz, R. Shintaku, and F. Gao, "Frequency-adaptive network modeling for integrative simulation of natural and envelope waveforms in power systems and circuits," *IEEE Trans. Circuits Syst. I*, vol. 53, no. 12, pp. 2788–2803, Dec. 2006.

[20] F. Gao and K. Strunz, "Frequency-adaptive power system modeling for multiscale simulation of transients," *IEEE Trans. Power Syst.*, vol. 24, no. 2, pp. 561–571, May 2009.

[21] H. Ye and K. Strunz, "Multi-scale and frequency-dependent modeling of electric power transmission lines," *IEEE Trans. Power Del.*, vol. 33, no. 1, pp. 32–41, Feb. 2018.

[22] Y. Xia, Y. Chen, H. Ye, and K. Strunz, "Multi-scale induction machine modeling in the dq0 domain including main flux saturation," *IEEE Trans. Energy Convers.*, vol. 3, no. 2, pp. 652–664, Jun. 2019.

[23] H. Ye, B. Yue, X. Li, and K. Strunz, "Modeling and simulation of multi-scale transients for PMSG-based wind power systems," *Wind Energy*, vol. 20, no. 1, pp. 1349–1364, Mar. 2017.

[24] S. K. Mitra, *Digital Signal Processing: A Computer-Based Approach*, 2nd ed. New York, NY, USA: McGraw-Hill, 2001.

[25] R. Pena, J. C. Clare, and G. M. Asher, "Doubly fed induction generator using back-to-back PWM converters and its application to variable-speed wind-energy generation," *Proc. Inst. Elect. Eng. B*, vol. 143, no. 3, pp. 231–241, May 1996.

[26] B. Boukhezzar and H. Siguerdidjane, "Nonlinear control of a variable-speed wind turbine using a two-mass model," *IEEE Trans. Energy Convers.*, vol. 26, no. 1, pp. 149–162, Mar. 2011.

[27] M. Kuschke and K. Strunz, "Energy-efficient dynamic drive control for wind power conversion with PMSG: Modeling and application of transfer function analysis," *IEEE J. Emerg. Sel. Topics Power Electron.*, vol. 2, no. 1, pp. 35–46, Mar. 2014.

[28] A. Yazdani and R. Iravani, *Voltage-Sourced Converters in Power Systems: Modeling, Control, and Applications*. Hoboken, NJ, USA: Wiley, 2010.

[29] S. Chiniforoosh *et al.*, "Definitions and applications of dynamic average models for analysis of power systems," *IEEE Trans. Power Del.*, vol. 25, no. 4, pp. 2655–2669, Oct. 2010.

[30] F. Gao and K. Strunz, "Multi-scale simulation of multi-machine power systems," *Int. J. Elect. Power Energy Syst.*, vol. 31, no. 9, pp. 538–545, Oct. 2009.

[31] S. Lefebvre and J. Mahseredjian, "Improved control systems simulation in the EMTP through compensation," *IEEE Trans. Power Del.*, vol. 9, no. 3, pp. 1654–1662, Jul. 1994.

[32] W. Gautschi, *Numerical Analysis: An Introduction*. Boston, MA, USA: Birkhauser, 1997.

[33] M. Kayikçi and J. V. Milanovic, "Assessing transient response of DFIG-based wind plants-the influence of model simplifications and parameters," *IEEE Trans. Power Syst.*, vol. 23, no. 2, pp. 545–554, May 2008.

[34] R. Teodorescu, M. Liserre, and P. Rodriguez, *Grid Converters for Photovoltaic and Wind Power Systems*. New York, NY, USA: Wiley, 2011.
[35] A. Yunus, M. A. Masoum, and A. Abu-Siada, "Application of SMES to enhance the dynamic performance of DFIG during voltage sag and swell," *IEEE Trans. Appl. Supercond.*, vol. 22, no. 4, Aug. 2012, Art. no. 5702009.
[36] H. Mohammadpour, S. G. Zadeh, and S. Tohidi, "Symmetrical and asymmetrical low-voltage ride through of doubly-fed induction generator wind turbines using gate controlled series capacitor," *IET Renew. Power Gener.*, vol. 9, no. 7, pp. 840–846, 2015.

Yue Xia received the B.S. and M.S. degrees from China Agricultural University, Beijing, China, in 2009 and 2011, respectively, and the Ph.D. degree from the Technische Universität Berlin, Berlin, Germany, in 2016, all in electrical engineering. From 2017 to 2019, he held a Postdoctoral Position with the Department of Electrical Engineering and Applied Electronic Technology, Tsinghua University, Beijing, China.

He is currently an Associate Professor with the College of Information and Electrical Engineering, China Agricultural University, Beijing, China. His research interests include power electronic systems, electrical machines, wind power, and modeling and simulation of power system transients.

Ying Chen (M'07) received his B.E. and Ph.D. degrees in electrical engineering from Tsinghua University, Beijing, China, in 2001 and 2006, respectively.

He is currently an Associate Professor with the Department of Electrical Engineering and Applied Electronic Technology, Tsinghua University. His research interests include parallel and distributed computing, electromagnetic transient simulation, cyber-physical system modeling, and cyber security of smart grid.

Yankan Song received the Ph.D. degree in electrical engineering from Tsinghua University, Beijing, China, in 2018.

He is currently a Postdoctoral Research Assistant with the Department of Electrical Engineering and Applied Electronic Technology, Tsinghua University. He is also the head of research with the Research Center of Cloud Simulation and Intelligent Decision-making, Energy Internet Research Institute, Tsinghua University. His research interests include power system modeling, electromagnetic transient simulation, parallel computing, and hybrid simulation of interconnected ac–dc systems.

Kai Strunz received the Dipl.-Ing. and Dr.-Ing. degrees (*summa cum laude*) from the Saarland University, Saarbrücken, Germany, in 1996 and 2001, respectively. He was with Brunel University, London, U.K., from 1995 to 1997. From 1997 to 2002, he was with the Division Recherche et Dévelopment of Electricité de France, Paris, France. From 2002 to 2007, he was an Assistant Professor of electrical engineering with the University of Washington, Seattle, WA, USA. Since 2007, he has been a Professor for Sustainable Electric Networks and Sources of Energy with Technische Universität Berlin, Berlin, Germany.

Dr. Strunz was the Chairman of the Conference IEEE PES Innovative Smart Grid Technologies, TU Berlin, in 2012. He is a Chairman of the IEEE Power and Energy Society Subcommittee on Distributed Energy Resources and Past Chairman of the Subcommittee on Research in Education. On behalf of the Intergovernmental Panel on Climate Change, he acted as a Review Editor for the Special Report on Renewable Energy Sources and Climate Change Mitigation. He received the IEEE PES Prize Paper Award in 2015 and the Journal of Emerging and Selected Topics in Power Electronics First Prize Paper Award 2015.